

Kinematics of outer halo globular clusters: M 75 and NGC 6426[★]

Andreas Koch¹, Michael Hanke¹, and Nikolay Kacharov²

¹ Zentrum für Astronomie der Universität Heidelberg, Astronomisches Rechen-Institut, Mönchhofstr. 12, 69120 Heidelberg, Germany

² Max-Planck-Institut für Astronomie, Königstuhl 17, 69117 Heidelberg, Germany

ABSTRACT

Globular clusters (GCs) and their dynamic interactions with the Galactic components provide an important insight into the structure and formation of the early Milky Way. Here, we present a kinematic study of two outer halo GCs based on a combination of VLT/FORS2, VLT/FLAMES, and Magellan/MIKE low- and high-resolution spectroscopy of 32 and 27 member stars, respectively. Although both clusters are located at Galactocentric distances of 15 kpc, they have otherwise very different properties. M 75 is a luminous and metal-rich system at $[\text{Fe}/\text{H}] = -1.2$ dex, a value that we confirm from the calcium triplet region. This GC shows mild evidence for rotation with an amplitude of $A_{\text{rot}} \sim 5 \text{ km s}^{-1}$. One of the most metal-poor GCs in the Milky Way (at $[\text{Fe II}/\text{H}] = -2.3$ dex), NGC 6426 exhibits marginal evidence of internal rotation at the 2 km s^{-1} level. Both objects have velocity dispersions that are consistent with their luminosity. Although limited by small-number statistics, the resulting limits on their A_{rot}/σ_0 ratios suggest that M 75 is a slow rotator driven by internal dynamics rather than being effected by the weak Galactic tides at its large distances. Here, M 75 ($A_{\text{rot}}/\sigma = 0.31$) is fully consistent with the properties of other, younger halo clusters. At $A_{\text{rot}}/\sigma_0 = 0.8 \pm 0.4$, NGC 6426 appears to have a remarkably ordered internal motion for its low metallicity, but the large uncertainty does not allow for an unambiguous categorization as a fast rotator. An accretion origin of M 75 cannot be excluded, based on the eccentric orbit, which we derived from the recent data release 2 of Gaia, and considering its younger age.

Key words. Globular clusters: individual: M 75, NGC 6426 — Galaxy: halo — Galaxy: kinematics and dynamics — Galaxy: structure

1. Introduction

Being amongst the oldest stellar systems in the universe, globular clusters (GCs) are ideal tracers of the earliest phases of the Milky Way's assembly. A particular emphasis lies on objects at large Galactocentric distances, as they probe the outermost halo and its accreted, ex-situ origin (Searle & Zinn 1978; Hartwick 1987; Carollo et al. 2007; Pillepich et al. 2015), or the important transition region between the inner and outer Galactic halo. Despite their, on average, younger ages (Mackey & Gilmore 2004; Marín-Franch et al. 2009), outer halo GCs are chemically very similar to halo clusters at smaller Galactocentric radii (Koch et al. 2009; Koch & Côté 2010; Çalişkan et al. 2012).

Internally, GCs are ever more deviating from the historic view of simple stellar populations. Similarly, spherical symmetry and dynamic equilibrium are often too simplistic assumptions for many of these objects. It is nowadays well established that these object host multiple populations, indicating a great degree of complexity during their early formation epochs (Decressin et al. 2007; D'Ercole et al. 2008; Bastian et al. 2013; Milone et al. 2017; Martocchia et al. 2018), as is presently most pronounced in terms of their light chemical abundance variations (Osborn 1971; Kayser et al. 2008; Carretta et al. 2009b; Gratton et al. 2012). However, none of the models presents a fully sat-

isfactory formation picture, yet (Bastian et al. 2015; Bastian & Lardo 2017).

In this context, a spatial segregation between first and second generations of stars has been observed (e.g., Carretta et al. 2010a), which is often accompanied by differences in their internal kinematics such as significantly different velocity dispersions and rotational amplitudes (Bellazzini et al. 2012). Furthermore, systematic correlations of the kinematic properties with other GC-characteristics, such as their metallicity or age have been reported (Carretta et al. 2010b; Bellazzini et al. 2012; Kacharov et al. 2014; Lardo et al. 2015). All these can be considered an imprint of the GCs' formation history rather than being a result of long-term dynamical evolution, so that detailed dynamical models are in place (Bianchini et al. 2013; Vesperini et al. 2013; Cordero et al. 2017; Baumgardt 2017). Rotation has by now been observed in most GCs and it leads to their morphological flattening, although also external effects such as pressure anisotropy and the Galactic tidal field can play a significant role in affecting the dynamical evolution and shape of these systems (e.g., Tiongco et al. 2018). Observationally, systematic monitoring of the internal dynamics of GCs has started blooming owing to the large multiplexing capacities of multi-object spectrographs and with the latest developments in integral-field unit spectroscopy (e.g., Kamann et al. 2018; Ferraro et al. 2018).

In this paper, we determine the kinematic properties of two GCs that do not have many common characteristics (such as metallicity or mass) except for their location in the transition region between the inner and outer Galactic halos, at $R_{\text{GC}}=14.4$ and 14.6 kpc, respectively. M 75 (\equiv NGC 6864) is a massive, metal-rich ($[\text{Fe}/\text{H}]=-1.2$ dex) GC that exhibits an extraordinary, trimodal horizontal branch (HB) morphology (Catelan et al. 2002; Kacharov et al. 2013). In contrast, the chemical abun-

Send offprint requests to: A. Koch; e-mail: andreas.koch@uni-heidelberg.de

[★] Based on observations collected at the European Southern Observatory under proposals 69.B-0305 (P.I. E. Tolstoy) and proposal 99.B-0012 (P.I. A. Koch). This paper includes data gathered with the 6.5 meter Magellan/Clay Telescope located at Las Campanas Observatory, Chile.

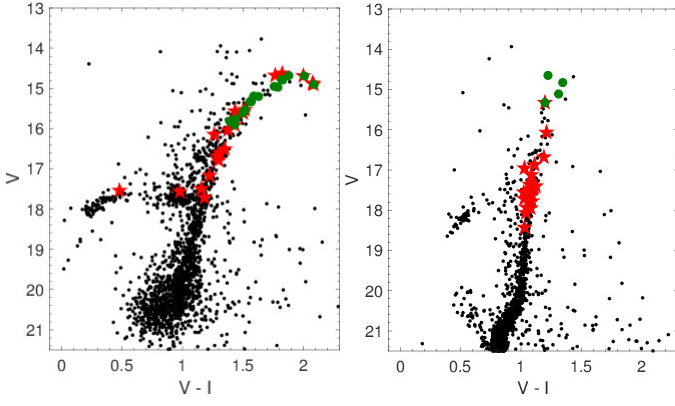


Fig. 1. Left: CMD of M75 from Kravtsov et al. (2007) with spectroscopic targets shown as red star symbols (FORS members), and green circles (MIKE targets). Right: CMD of NGC 6426 from the HST photometry of Dotter et al. (2011), indicating member candidates (red stars). Here, green circles show the four stars studied in high resolution by Hanke et al. (2017).

dance study of Kacharov et al. (2013) revealed only moderate light element anti-correlations, lacking a third, “extreme” component that would go in lockstep with the extended, hot HB, concluding that this object’s HB peculiarity has been shaped by processes that are yet unknown. On the other hand, the low-mass NGC 6426 is one of the three most metal-poor and oldest GCs in the Milky Way system (Salaris & Weiss 2002; Hanke et al. 2017). Owing to a limited spectral sample, Hanke et al. (2017) could not establish the presence of a Na-O anti-correlation in NGC 6426, but mild variations in other elements suggested that multiple populations are also likely present in this object. Both our target clusters are, kinematically, hitherto uncharted.

This paper is organized as follows: Sect. 2 presents the data and our velocity measurements. Additional measurements of metallicities for the M75 stars are briefly discussed in Sect. 3, before describing the general kinematic properties of the two GCs in Sect. 4. Next, Sect. 5 focuses on an in-depth analysis of the clusters’ internal rotation, before discussing our findings in Sect. 6.

2. Data and radial velocity measurements

2.1. M75: MIKE high-resolution spectra

The spectra used in the present analysis are those already presented in Kacharov et al. (2013). In brief, high-resolution ($R \sim 40,000$) spectra of 18 red giant member stars have been obtained with the Magellan Inamori Kyocera Echelle (MIKE) spectrograph at the 6.5-m Magellan2/Clay Telescope at Las Campanas Observatory, Chile. Out of these, 16 had a sufficient signal-to-noise ratio (SNR) for a detailed abundance analysis. We measured their radial velocities via a cross-correlation of the spectra against a synthetic template of a red giant branch (RGB) star of stellar parameters typical of the observed sample.

2.2. M75: VLT/FORS2 low-resolution data

Low-resolution spectroscopy of 37 stars within $3.8'$ (7.5 half-light radii r_h) of the GC is available from the ESO archive. The location of these targets in a colour magnitude diagram (CMD) is shown in Fig. 1. These spectroscopic data have been taken during one night in Aug 2002 with the Focal Reducer and low dispersion Spectrograph FORS2 at the Very Large Telescope (VLT)

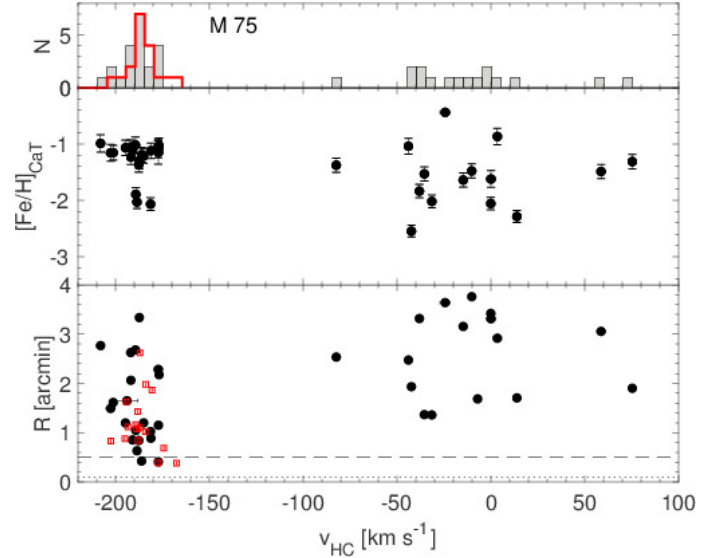


Fig. 2. Heliocentric radial velocity against radial distance (bottom panel) and CaT-based metallicity (middle) from the FORS data are shown in black. The histogram in the top panel indicates the peak of M75 at -188 km s^{-1} , and the dotted and dashed lines in the bottom panel show the cluster’s core- and half-light radii. Red symbols in the bottom panel and the red solid line in the histogram plot refer to the MIKE sample.

under proposal 69.B-0305 (P.I. E. Tolstoy). The filter used was OG590 with grism 1028z, centered around the near-infrared calcium triplet (CaT) lines at $\sim 8500 \text{ \AA}$, and the exposure time was $2 \times 900 \text{ s}$. These data were reduced using IRAF’s *apall* and other standard routines (see also Fraternali et al. 2009) and have a resolving power of ~ 2500 , as determined from the width of the sky emission lines. Typical SNR values range from $7\text{--}120 \text{ pixel}^{-1}$, with a median of $\sim 70 \text{ pixel}^{-1}$.

Heliocentric velocities of the target stars were determined by cross correlation (within IRAF’s *fxcor*) against a synthetic spectrum of the three CaT lines, adopted as simple Gaussian profiles (Kleyna et al. 2004). One of the stars is a blue HB star and we measured its velocity from the Doppler shifts of the prominent, broad Paschen lines, yielding a larger uncertainty. The formal errors returned by *fxcor* are of the order of 1.5 km s^{-1} . As a result (Fig. 2), we find 21 stars within $3.3'$ ($6.7 r_h$) with velocities below -150 km s^{-1} that are clearly separated from the bulk of Galactic foreground stars. We therefore assume these as GC member candidates. Their properties are listed in Table 1 and Fig. 1 shows their spatial distribution and velocity histogram.

The lay-out of FORS2 with its two separate CCD chips can, in principle, lead to systematic offsets in radial velocities if measured on different chips (e.g., Fraternali et al. 2009). In order to ascertain that our data are not affected by such systematics, we computed the kinematics of the subsamples from chip 1 and 2 separately and find only a marginal (0.7σ) difference of the mean systemic velocity as computed from either chip. We deem chip-offsets redundant for the remainder of this work and will further comment on this option in the sections presenting our results below.

2.3. M75: Combined sample

In the following, we determined mean heliocentric radial velocities and velocity dispersions in a maximum likelihood sense, by optimizing the probability \mathcal{L} that the given ensemble of stars

Table 1. Properties of M 75 member stars.

ID ^a	α (J2000.0)	δ	B [mag]	V [mag]	I [mag]	v_{HC} [km s ⁻¹] FORS2	MIKE	ΣW [mÅ]	[Fe/H] _{CaT} [dex]	Type
652	20 05 56.35	-21 54 35.49	16.42	14.63	12.80	-191.8±1.0	...	5.75±0.10	-1.08±0.12	RGB
583	20 06 07.96	-21 54 52.81	16.34	14.68	12.91	-187.6±0.6	-188.1±0.1	5.43±0.11	-1.20±0.12	RGB
528	20 06 00.24	-21 55 12.57	16.70	14.69	12.68	-189.2±0.7	-188.7±0.2	4.33±0.09	-1.66±0.10	RGB
461	20 06 03.80	-21 55 34.60	16.62	14.78	12.96	...	-167.5±0.1	RGB
503	20 06 10.89	-21 55 23.10	16.69	14.79	12.96	...	-188.3±0.1	RGB
391	20 06 05.47	-21 55 52.82	16.82	14.87	12.79	-188.6±0.7	...	3.92±0.09	-1.78±0.10	RGB
1307	20 06 02.83	-21 54 20.98	16.93	14.90	12.81	-181.3±1.7	-184.1±0.2	3.83±0.08	-1.81±0.10	RGB
1312	20 06 06.79	-21 54 15.90	16.73	14.95	13.19	...	-187.2±0.1	RGB
251	20 05 58.88	-21 56 42.30	16.78	14.97	13.18	...	-183.9±0.1	RGB
1459	20 06 03.19	-21 56 19.60	16.74	15.19	13.60	...	-193.5±0.1	RGB
442	20 06 07.18	-21 55 39.80	16.92	15.30	13.73	...	-174.3±0.1	RGB
901	20 06 17.33	-21 52 20.90	16.90	15.20	13.57	...	-184.2±0.1	RGB
483	20 06 22.55	-21 55 29.30	16.94	15.33	13.77	...	-186.5±0.1	RGB
655	20 06 08.80	-21 54 34.90	16.93	15.33	13.76	...	-189.4±0.1	RGB
239	20 06 02.23	-21 56 46.35	17.02	15.53	14.01	-201.2±1.6	-194.3±0.1	5.34±0.08	-1.01±0.12	RGB
1251	20 06 06.21	-21 55 02.56	17.08	15.59	14.09	-177.2±1.8	-177.1±0.1	5.53±0.08	-0.92±0.12	RGB
512	20 06 01.08	-21 55 19.81	17.08	15.61	14.11	-191.0±0.5	-195.1±0.1	5.37±0.10	-0.97±0.12	RGB
486	20 06 12.76	-21 55 27.40	17.22	15.76	14.32	...	-180.6±0.1	RGB
612	20 06 01.89	-21 54 46.30	17.15	15.81	14.42	...	-202.6±0.1	RGB
876	20 06 08.04	-21 52 45.44	17.34	15.91	14.48	-191.9±1.5	-187.0±0.1	5.28±0.09	-0.93±0.12	RGB
1464	20 06 06.28	-21 56 05.02	17.38	16.03	14.66	-181.2±1.1	...	5.09±0.10	-0.98±0.12	RGB
732	20 06 06.40	-21 54 11.12	17.82	16.50	15.15	-177.2±1.8	...	4.84±0.19	-0.96±0.14	RGB
1286	20 06 00.16	-21 54 43.45	17.86	16.62	15.31	-194.7±0.7	...	4.83±0.09	-0.93±0.12	RGB
887	20 06 06.12	-21 52 36.51	17.91	16.68	15.39	-189.4±0.9	...	4.89±0.11	-0.89±0.13	RGB
827	20 06 09.62	-21 53 24.57	18.04	16.79	15.49	-176.8±1.5	...	4.80±0.08	-0.90±0.12	RGB
856	20 06 02.76	-21 53 02.00	18.30	17.16	15.94	-177.2±2.2	...	4.30±0.39	-1.01±0.20	RGB
783	20 06 04.79	-21 53 46.71	18.58	17.49	16.34	-202.6±2.4	...	4.08±0.18	-1.01±0.14	RGB
1115	20 05 58.10	-21 57 34.05	18.76	17.71	16.53	-208.0±2.1	...	4.29±0.20	-0.87±0.14	RGB
438	20 06 04.29	-21 55 40.83	17.03	15.56	14.13	-186.1±0.6	...	5.24±0.09	-1.04±0.12	AGB
1152	20 06 07.84	-21 56 13.84	17.36	16.15	14.88	-185.0±0.9	...	4.82±0.09	-1.06±0.12	AGB
1106	20 06 13.08	-21 57 59.43	18.46	17.57	16.59	-187.3±1.1	...	3.72±0.15	-1.14±0.13	RHB
1328	20 06 09.09	-21 53 57.87	17.93	17.54	17.06	-193.9±5.9	BHB

^a Taken from Kravtsov et al. (2007)

with velocities v_i and errors σ_i are drawn from a population with mean velocity $\langle v \rangle$ and dispersion σ (e.g., Walker et al. 2006):

$$\mathcal{L} = \prod_{i=1}^N \left(2\pi(\sigma_i^2 + \sigma^2) \right)^{-\frac{1}{2}} \exp \left(-\frac{(v_i - \langle v \rangle)^2}{2(\sigma_i^2 + \sigma^2)} \right) \quad (1)$$

From the 21 stars observed with FORS alone, we thus derive a mean heliocentric radial velocity of $-188.4 \pm 1.8 \text{ km s}^{-1}$ and a velocity dispersion σ of $8.1 \pm 1.3 \text{ km s}^{-1}$, both of which are consistent with earlier results (Pryor & Meylan 1993; Harris 2010). Similarly, the MIKE sample of 18 stars returns a value of $-186.2 \pm 1.9 \text{ km s}^{-1}$ with dispersion of $7.8 \pm 1.3 \text{ km s}^{-1}$, in excellent agreement with the aforementioned values.

Seven stars have been targeted in common between both campaigns. Here, the velocities agree excellently for three of those, while the difference is larger, up to 7 km s^{-1} for the remainder. Such inconsistencies could, in principle indicate that those stars are in binaries; however, the temporal sampling of the observing runs is insufficient to test for more systematic variations. Overall, the mean difference between the MIKE and FORS values is 0.7 km s^{-1} with a large scatter of 3.9 km s^{-1} . These deviations are independent on the stars' locations in the GC, their position in the CMD, and neither subset shows systematically lower or larger values alone.

To construct a final, *bona-fide* sample, we shifted the FORS velocities by the difference in mean velocity, thereby tying them

to the more precise MIKE scale. As a second test, we rejected those common stars with velocities that differ by more than the combined error bar and, for the remaining three overlapping stars, we computed an error-weighted mean value. We emphasize that the results of the kinematic analysis below are insensitive to the in- or exclusion of the common stars, or the employed combination scheme so that we will continue with the sample after shifting to a common velocity scale and removal of the binary candidates (see also Koch et al. 2007).

2.4. NGC 6426: VLT/FLAMES

The central regions of this GC are heavily affected by crowding, which is unfortunate for efficient multi-object fibre spectroscopy. For target selection, we relied on infrared photometry from the Two Micron All Sky Survey (2MASS; Cutri et al. 2003). Furthermore, Hubble Space Telescope (HST) photometry is available in V and I for a pencil beam toward this GC (Dotter et al. 2011), which contains most of our target stars. The corresponding CMD is shown in the right panel of Fig. 1.

The observations were carried out using the HR13 grating of the GIRAFFE spectrograph as part of the Fibre Large Array Multi Element Spectrograph (FLAMES; Pasquini et al. 2002) at the ESO/VLT. This setting provides a wavelength coverage of

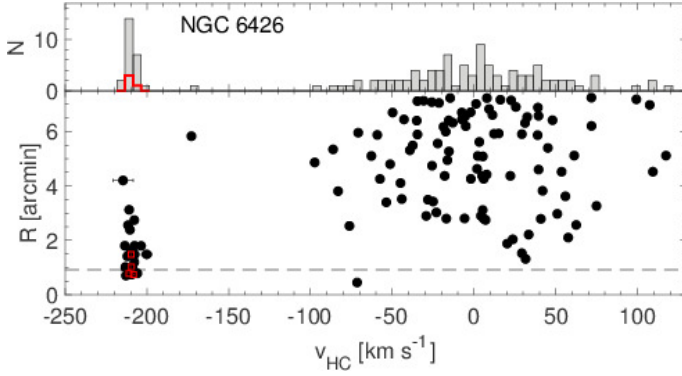


Fig. 3. Heliocentric radial velocity against radial distance (bottom panel) for the entire NGC 6426 observations. The histogram in the top panel indicates the peak of the GC at -210 km s^{-1} . The dashed line in the bottom panel shows the cluster’s half-light radius. Red symbols and the red histogram refer to the MIKE sample of Hanke et al. (2017).

6100–6400 Å at a resolving power of 20,000, where 125 fibres were placed on stars.

After the loss of two entire runs over two ESO periods due to bad weather, data could finally be accrued on the two nights of Aug. 21 and Sep. 19, 2017. While originally conceived as an abundance-project, only two out of the six granted observing blocks were taken, which are the base for the present, kinematic study, for which the lower SNR is sufficient. Here, the total exposure time was 1.4 hours, split into $4 \times 1240 \text{ s}$ exposures. The data were reduced using ESO standard routines.

As above, we measured radial velocities from a cross-correlation of the spectra against a synthetic template spectrum with stellar parameters representative of the target stars. The errors returned by *fxcor* were re-scaled using the (up to four) repeat observations following the formalism of Vogt et al. (1995) and Koch et al. (2007), resulting in a median velocity error of 1.5 km s^{-1} . The resulting measurements and target properties are listed in Table 2.

The plot of velocity vs. radial distance from the cluster center in Fig. 3 shows a clear signal of the GC population at a heliocentric velocity of $-209.7 \pm 0.5 \text{ km s}^{-1}$ that is significantly detached from the Milky Way foreground. This value is considerably lower than that listed in the Harris (2010) catalogue based on low-resolution spectra of a handful of stars. As for M 75, we also combined our sample with the MIKE data of (Hanke et al. 2017) by shifting the FLAMES velocities to the higher-resolution MIKE scale. This yields a final sample of 27 member candidates with a dispersion of $1.9 \pm 0.4 \text{ km s}^{-1}$, and we discuss their kinematic properties in the following.

3. M 75: Calcium Triplet metallicities

As a more detailed chemical abundance analysis of this GC exists from the MIKE spectra of Kacharov et al. (2013), here, we determined the equivalent widths (EWs) of the CaT lines from the FORS2 spectra as another means of membership assessment. To this end, we fitted Gaussian plus Lorentz line profiles (Cole et al. 2004) to each line using line and continuum band passes from Armandroff & Zinn (1988). Adopting the calibrations of line strength onto metallicity by Rutledge et al. (1997a,b), we find that 18 of the 21 likely radial velocity members also cluster in abundance space (Fig. 2, middle panel) around $[\text{Fe}/\text{H}]_{\text{CaT}} = -1.1 \text{ dex}$ on the scale Carretta et al. (2009a). This compares favourably with previous photometric estimates

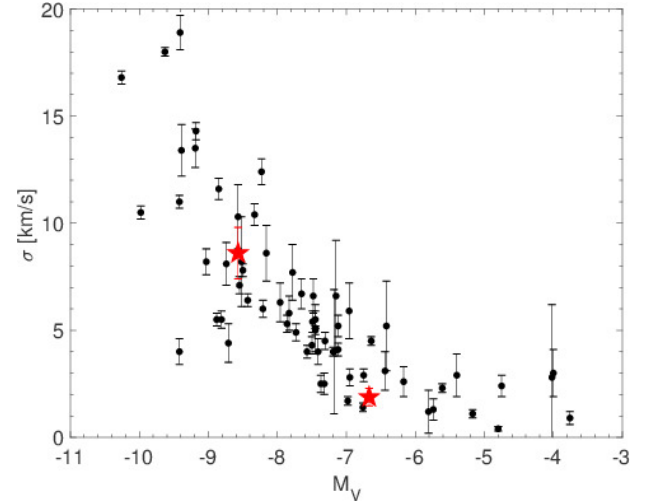


Fig. 4. Global velocity dispersion vs. absolute magnitude, using data from Pryor & Meylan (1993) and Harris (2010), and with the latest measurements of low-mass GCs from Koch et al. (2017a,b, 2018). Targets of this study are indicated by red stars.

of -0.7 to -1.3 dex (Catelan et al. 2002; Kravtsov et al. 2007; Kacharov et al. 2013). The other three stars with lower metallicities at M 75’s systemic velocity can still be considered likely members: these are the reddest bright objects at $V-I > 1.9 \text{ mag}$. Given the inflection of this metal-rich GC’s RGB near the tip these are likely luminous AGB stars with notably narrow (CaT) absorption lines, for which the linear CaT calibration becomes unreliable (e.g., Garnavich et al. 1994). Moreover, the data of Corwin et al. (2003) indicate that, at least two out of these three, are variable stars.

As a result, the mean metallicity of $-1.00 \pm 0.04 \text{ dex}$ with an intrinsic dispersion of $0.07 \pm 0.05 \text{ dex}$ is slightly more metal-rich than the high-resolution, high-SNR MIKE study of Kacharov et al. (2013), who found a mean $[\text{Fe I}/\text{H}]$ of -1.16 ± 0.02 . This systematic over-estimate from the low-resolution FORS2 spectra is also seen in the one-to-one comparison of the stars that overlap between the both samples. This discrepancy is considerably alleviated when comparing our results to the metallicity scale from ionized iron lines: here, Kacharov et al. (2013) find a GC mean of $[\text{Fe II}/\text{H}] = -0.98 \pm 0.03 \text{ dex (random)} \pm 0.16 \text{ dex (systematic)}$ with a 1σ spread of 0.13 dex , which is fully compatible with our present finding. This strongly attests to favouring the use of Fe II as a prime metallicity scale (e.g., Kraft & Ivans 2003; Hanke et al. 2017), as it is also less prone to NLTE-effects.

4. General kinematics

Based on our measurement of 32 (27) heliocentric velocities in M 75 and NGC 6426, respectively, we determined the global kinematic properties of the GCs (as listed in Table 3) from the *bona fide*, combined samples.

For M 75, we determined a mean heliocentric velocity of $-186.2 \pm 1.5 \text{ km s}^{-1}$ with a velocity dispersion of $8.2 \pm 1.1 \text{ km s}^{-1}$. While this dispersion seems high for a GC at a first glance, it has to be kept in mind that M 75 is a massive system so that our measured value is to be expected and fully compatible with the high values for σ found in other luminous, dense systems (Fig. 4; Pryor & Meylan 1993).

For NGC 6426, we find a mean velocity and dispersion of $-209.7 \pm 0.4 \text{ km s}^{-1}$ and $1.9 \pm 0.4 \text{ km s}^{-1}$, respectively. The low, latter value is in line with this GC’s lower mass, as also sug-

Table 2. Properties of the NGC 6426 member stars from FLAMES

ID ^a	α (J2000.0)	δ	V [mag]	V-I [mag]	K [mag]	J-K [mag]	SNR [px ⁻¹]	v_{HC} [km s ⁻¹]	r [']
385 ^b	17:44:56.70	3:09:39.34	15.327	1.20	12.302	0.80	51	-209.2±0.9	0.74
777	17:44:56.81	3:10:47.54	16.067	1.21	12.991	0.82	42	-205.9±0.6	0.78
2075	17:44:52.09	3:09:40.69	16.681	1.19	13.819	0.70	35	-208.1±0.9	0.84
1198	17:44:52.85	3:09:18.07	16.868	1.11	14.008	0.68	30	-213.2±0.9	1.02
168	17:44:49.00	3:09:06.44	16.956	1.03	14.384	0.76	26	-213.5±1.4	1.80
1961	17:44:57.21	3:08:56.39	17.125	1.09	14.413	0.70	25	-212.1±1.2	1.41
196	17:44:53.02	3:11:19.68	17.359	1.07	14.728	0.53	21	-207.8±1.3	1.20
1898	17:44:56.52	3:11:37.31	17.369	1.08	14.648	0.80	20	-200.1±3.0	1.48
618	17:44:53.04	3:10:49.33	17.401	1.12	14.637	0.76	17	-211.3±1.2	0.74
842	17:44:55.54	3:11:09.23	17.417	1.10	14.519	0.82	20	-208.7±2.1	0.97
919	17:44:54.14	3:09:23.30	17.448	1.10	14.581	0.76	19	-210.4±1.2	0.83
2169	17:44:48.34	3:09:22.05	17.553	1.02	15.016	0.82	19	-207.6±1.5	1.80
328	17:44:57.24	3:09:54.03	17.626	1.09	14.819	0.82	19	-212.9±1.5	0.70
494	17:45:00.17	3:11:22.72	17.716	1.03	15.098	0.74	15	-203.6±2.7	1.80
1211	17:44:51.41	3:10:18.61	17.776	1.09	15.127	0.74	13	-210.5±2.1	0.83
1575	17:44:51.26	3:11:24.78	17.929	1.04	15.287	0.70	9	-207.5±4.6	1.48
268	17:44:49.30	3:11:07.77	17.948	1.08	15.322	0.62	14	-209.7±2.9	1.63
1908	17:44:58.00	3:10:46.77	18.065	1.04	15.526	0.59	15	-209.2±1.4	1.00
366	17:44:51.03	3:10:03.70	18.430	1.03	15.526	0.72	11	-211.6±4.2	0.93
89	17:44:43.82	3:07:00.26	14.903	0.71	5	-214.6±6.3	4.20
162	17:44:42.53	3:10:55.34	14.157	0.70	28	-210.9±1.9	3.12
995	17:44:53.75	3:12:56.49	15.140	0.77	15	-207.8±2.2	2.74
1159	17:44:50.69	3:08:02.66	15.588	0.56	17	-210.4±1.7	2.39
1529	17:45:04.71	3:09:39.16	15.065	0.57	18	-211.6±1.4	2.56

Notes. ^(a) IDs based on our 2MASS input catalog. ^(b) This is star 14853 in Hanke et al. (2017).

Table 3. Global and kinematic properties of the two targeted GCs

Parameter	Value		Reference ^b
	M 75	NGC 6426	
l [°]	20.30	28.09	1
b [°]	-25.75	16.23	1
R_{GC} [kpc]	14.7	14.4	1
R_{\odot} [kpc]	20.9	20.6	1
r_h [']	0.46	0.92	1
r_t [']	5.7	13.0	1
[Fe/H]	-1.13/-1.16	-2.34	2,3,4
N^a	32	27	2,4
v_{HC} [km s ⁻¹]	-186.2±1.5	-209.7±0.5	2
σ [km s ⁻¹]	8.2±1.1	1.9±0.4	2
A [km s ⁻¹]	5.0±0.9	3.9±1.8	2
PA [°]	-15±30	281 ⁺³⁶ ₋₂₅	2
A_{rot} [km s ⁻¹]	4.5±2.1	2.0 ^{+1.1} _{-0.9}	2; Eq. 2
R_{peak} [']	1.6 ^{+1.6} _{-1.1}	2.1 ^{+1.5} _{-1.2}	2; Eq. 2
σ_0 [km s ⁻¹]	14.1 ^{+2.4} _{-2.0}	2.4 ^{+0.7} _{-0.5}	2; Eq. 3
$\mu_{\alpha \cos \delta}$ [mas yr ⁻¹]	-0.39 ^{+0.79} _{-0.63}	-1.82 ^{+0.31} _{-0.34}	2,5
μ_{δ} [mas yr ⁻¹]	-2.76 ^{+0.52} _{-0.60}	-2.98 ^{+0.34} _{-0.38}	2,5

Notes. ^(a) Number of member stars in the respective analysis
^(b) References: (1): Harris (2010); (2): This work; (3): Kacharov et al. (2013); (4): Hanke et al. (2017); (5): Gaia Collaboration et al. (2018a).

gested by Fig. 4. Hanke et al. (2017) found a mean systemic velocity that is lower by 2.4 ± 0.8 km s⁻¹ that was, however, based on four stars. Accordingly, their velocity dispersion is considerably lower than our value, at 1.0 ± 0.4 km s⁻¹. One star in the present sample is in common with Hanke et al. (2017). Here, the velocity from their MIKE spectra differs by 1.7 km s⁻¹ (1.2σ).

Since the latter work was focused on a high-resolution chemical abundance analysis, this discrepancy may hint at an underestimation of the velocity errors, which were not crucial for the chemical purpose. Likewise, the different result by Dias et al. (2015) of a mean velocity of -242 ± 11 km s⁻¹ can be understood in terms of the small sample size (at five stars) and a low spectral resolution of $R \sim 2000$.

Since Galactic foreground stars at similar velocities can, in principle, inflate velocity dispersion measurements and corrupt kinematic analyses (e.g., Walker et al. 2009), we estimated the amount of contamination via the Besançon Galaxy model (Robin et al. 2003). As a result we do not expect a single foreground interloper within the CMD selection criteria and at velocities below -100 km s⁻¹ drawn from samples like our NGC 6426 observations. The same holds for M 75.

5. Rotation analysis

As a first step, we followed the standard procedure of dividing the data into bins of position angle and computing the mean velocity of the respective subsamples (e.g., Koch et al. 2007; Kacharov et al. 2014). The resulting difference in mean velocity from either side of a line passing through the GC center at that angle then yields the projected rotation curves in Fig. 5. These can be described by a simplistic sinusoidal with amplitude A and position angle (PA, counting North through East) as $\Delta v = A \sin(\varphi + \text{PA})$, where φ is the position angle of each star with respect to the cluster center. As the spatial distribution of the stars in the bottom panel of Fig. 5 indicates, the main source of uncertainty in this analysis will be the small-number statistics of the samples.

Next we performed a more advanced Bayesian fit to the discrete kinematic data of the two GCs (Mackey et al. 2013, see also Kacharov et al. 2014), accounting simultaneously for both the

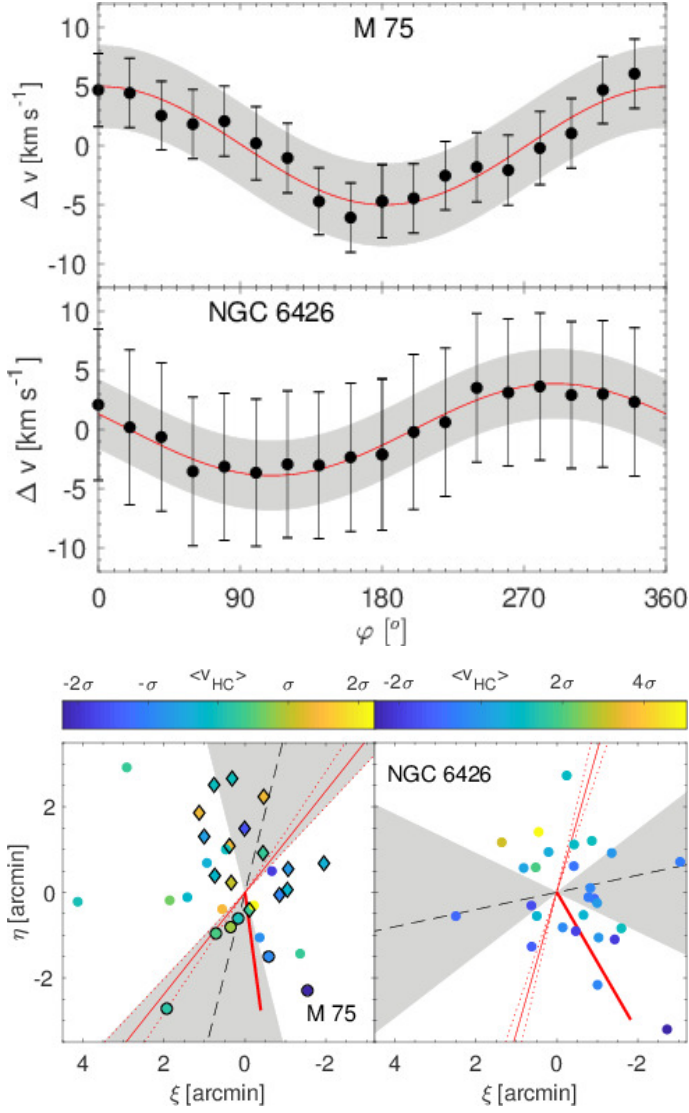


Fig. 5. Top panels: Rotation curves and best-fit sinusoidal for both GCs. The bottom panels show the location of the target stars, colour-coded by radial velocity in units of their dispersion. Here, diamonds refer to M 75 targets on chip #1 on FORS2, circles are stars on chip #2, and MIKE targets are shown without extra delimiters. The gray shaded areas indicate the error margin of the rotation axis, which itself is shown as a dashed line. Each clusters' major axis position angles from Chen & Chen (2010) are plotted as thin red lines; finally, the direction of the Gaia DR2 proper motion is shown via a thick red line.

rotation profile $V_{\text{rot}}(X_{\text{PA}})$ (Eq. 2) and velocity dispersion profile $\sigma(R)$ (Eq. 3). The former parameterization adopts a cylindrical rotation and violent relaxation. Overall, this approach and the associated likelihood distributions follows closely the method described by Cordero et al. (2017, their Eqs. 2,5).

$$V_{\text{rot}} \sin i = \frac{2 A_{\text{rot}}}{R_{\text{peak}}} \frac{X_{\text{PA}}}{1 + (X_{\text{PA}}/R_{\text{peak}})^2} \quad (2)$$

$$\sigma(R) = \sigma_0 \left(1 + (R/a)^2\right)^{-1/4} \quad (3)$$

The adopted dispersion model follows the prediction for a Plummer sphere with one free parameter – the central velocity dispersion σ_0 . We kept the half-mass radius a fixed at the half-light radius divided by a factor of 1.3.

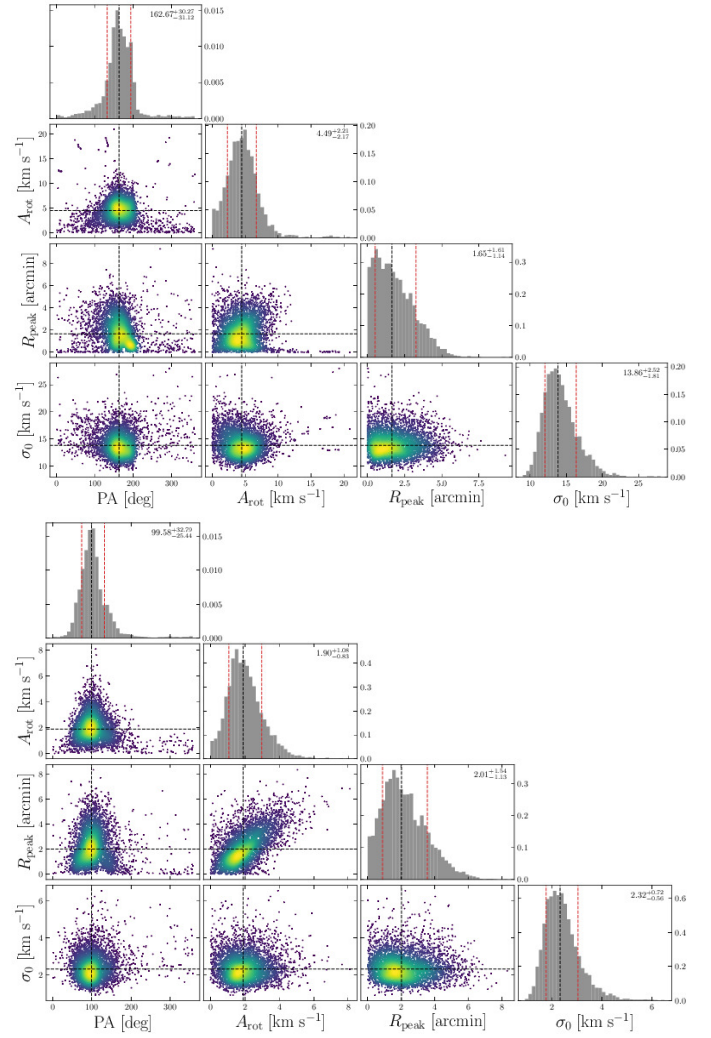


Fig. 6. Posterior probability distributions of our rotational analysis, with parameters as defined in Eqs. 1,2. The top and bottom panels show the results for M 75 and NGC 6426, respectively.

In contrast, the rotation parameterization has three free parameters: the position angle (PA) of the rotation axis, the amplitude of rotation (A_{rot}), and the distance of the peak rotation from the cluster's centre, X_{rot} . As per Eq. 2, this rotation curve is given as a function of the distance along the major axis, also accounting for the unknown inclination i . As we found that the position of the peak rotation is not well constrained by the data, we used a normal distribution with a mean at the cluster's centre and a standard deviation of $2'$ as a prior on this parameter. In practice, we sampled the joint posterior distribution of the four free parameters using the affine-invariant MCMC algorithm (Goodman & Weare 2010; Foreman-Mackey et al. 2013). The resulting posterior probability distributions are shown in Fig. 6, and in the following Section we summarize the resulting free parameters in terms of their median values and adopt the 15.9% and 84.1% percentiles as lower and upper error bounds. While the median values indicate a marginal level of rotation in either object, the full probability distributions suggest that an absence of rotation cannot be fully excluded.

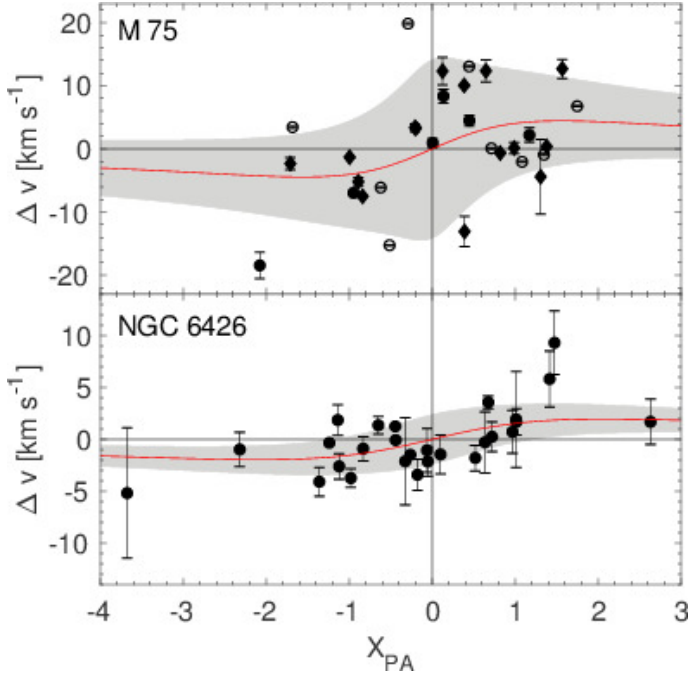


Fig. 7. Rotation curve and best-fit curve à la Eq. 2. The gray-shaded area indicates the margins imposed by the radial velocity dispersion profile (Eq. 3). Different symbols for M 75 reflect targets on different FORS2 chips (filled) and those observed with MIKE (open).

5.1. M 75

Our tests for rotation suggest that M 75’s rotation axis is inclined at a position angle of $-15^\circ \pm 30^\circ$. Using 2MASS photometry and density distributions, Chen & Chen (2010) determined the morphological parameters for almost the entire Galaxy’s GC population. For M 75, their study implied a major axis position angle¹ of $40 \pm 5^\circ$. Since morphological distortions would be manifest in a flattening that is aligned with the minor axis, we will consider in the following rather the minor axis position angle, which for M 75 is thus -50° . In this regard, our kinematic rotation axis is offset to the cluster’s minor axis by 35° , but it should be kept in mind that the actual flattening of M 75 is very small, at an axis ratio of 0.92 ± 0.03 (Chen & Chen 2010), and that our kinematic analysis is aggravated by small-number statistics. However, as the distinction in Fig. 5 (bottom left) of stars on the two FORS2 chips indicates, the preferential rotation direction is not aligned with the instrument so that chip-offsets are unlikely to be the cause of the rotation signal. This is bolstered by the independent confirmation of the additional MIKE data.

The amplitude of the sinusoidal in Fig. 4, which is statistically on the order of twice the overall average rotation signal (Bellazzini et al. 2012), is $A = 5.0 \pm 0.9 \text{ km s}^{-1}$, while the more detailed Bayesian fit of Eq. 2 to the non-binned profile yielded a half-amplitude of $A_{\text{rot}} = 4.5 \pm 2.1 \text{ km s}^{-1}$ around an axis that is offset from the center by some $1.6'$ (Fig. 7; Table 3). At the GC’s half-light radius of $0.5'$ (Harris 2010), this would correspond to three such radii and would be remarkably large. Considering the poor sampling of our data in the central regions of M 75, we do not interpret this value any further.

¹ We note that Chen & Chen (2010) reported their parameters in Galactic coordinates, leading to an original angle with respect to the North Galactic Pole of 148° .

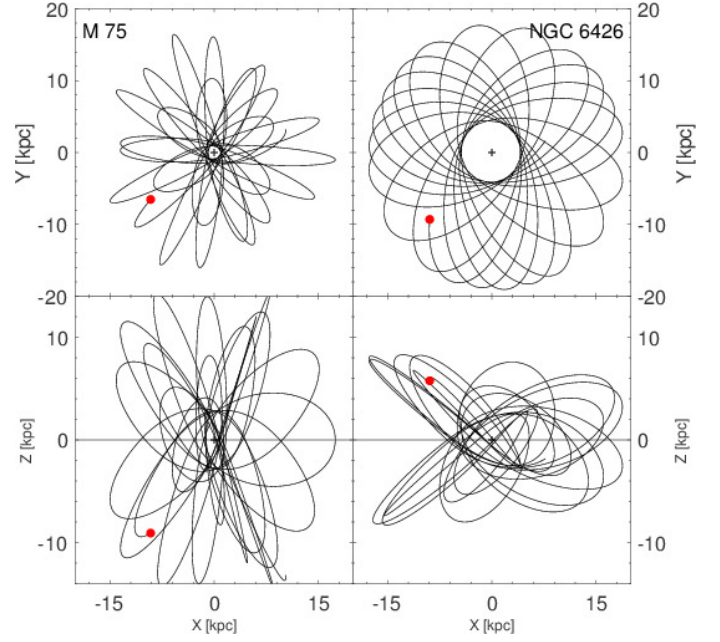


Fig. 8. Orbit projections as a result of a backward computation. Here, only a timeframe of 6 Gyr is depicted. The present location of the GCs is shown as red point. The cross and line denote the Galactic center and plane.

5.2. NGC 6426

The best-fit position angle for this GC is 281° . This compares to a *minor* axis position angle from the morphological analysis of Chen & Chen (2010) of $253^\circ \pm 3^\circ$, which is marginally consistent with our measurement. On the other hand, our derived amplitudes of $A = 3.9 \pm 1.8$ and $A_{\text{rot}} = 2.0^{+1.1}_{-0.9} \text{ km s}^{-1}$, the latter with a nominal peak at $2.1'^{+1.5}_{-1.2}$ (thus well outside the cluster core, at $r_c = 0.26'$), are clearly a limited representation of NGC 6426’s kinematics.

6. Orbits

In order to obtain the full kinematic information on our clusters, we derived their proper motions using the recent second data release, DR2, of Gaia (Gaia Collaboration et al. 2018a). To identify the *bona fide* cluster signature in proper motion space, we selected stars within 1.5 times r_h , vetting those with significant parallaxes as near-by foreground stars, and we demanded that the errors in either direction are $\sigma_\mu < 0.5 \text{ mas yr}^{-1}$. This way, we utilized 161 and 103 objects towards M 75 and NGC 6426, respectively. The resulting median values (with 15.9% and 84.1% percentile uncertainties) we find are $(\mu_\alpha \cos \delta, \mu_\delta) = (-0.4^{+0.8}_{-0.6}, -2.8^{+0.5}_{-0.6}) \text{ mas yr}^{-1}$ for M 75 and $(-1.8 \pm 0.3, -3.0^{+0.3}_{-0.4}) \text{ mas yr}^{-1}$ for NGC 6426. These values are in excellent agreement with the recent HST study of Sohn et al. (2018) for NGC 6426 and with the values for M 75 of Chemel et al. (2018), in turn based on a variety of surveys including Gaia DR1. It is interesting to note that, for M 75, the direction of motion is consistent with the rotation axis, while for NGC 6426 it is almost perpendicular. Our derived proper motions were then fed into the Galactic potential of Dehnen & Binney (1998), which contains contributions from the halo and disk, and spherical bulge. The orbital integrations were carried out backwards for 12 Gyr and the resulting projections are shown in Fig. 8.

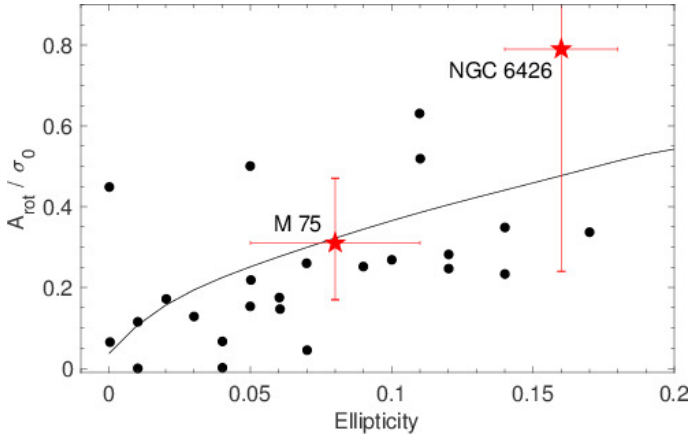


Fig. 9. Ratio of rotation amplitude and central velocity dispersion, according to Kacharov et al. (2014) with additional measurements from Bellazzini et al. (2012). The solid line is an isotropic rotating sphere as described by Binney (2005).

Both GCs show typical motions with apocenters of 17.5 kpc (M 75) and 19.4 kpc (NGC 6426) that lie close to their current Galactocentric distances. At 0.4 Gyr each, their orbital periods are fairly short. The eccentricities of these outer halo objects are large, at $e = 0.63$ for NGC 6426, and even more notably for M 75, which shows an eccentric orbit with $e=0.87$. The latter could indicate that M 75 has once been accreted, as also bolstered by its younger age compared to other GCs at similar metallicities (Catelan et al. 2002). However, while this object lies close in projection to the disrupted Sagittarius Stream, no tidal debris around M 75 has been observed (Carballo-Bello et al. 2014), and Majewski et al. (2004) argue that this GC is unlikely to be associated with Sagittarius based on its large approaching radial velocity. As for NGC 6426, Forbes & Bridges (2010) note that this GC lies close to the purported orbit of the Canis Major overdensity, but given our present result, we cannot unambiguously constrain an in- or ex-situ origin of this metal-poor object. Globally speaking, the full, three-dimensional kinematics of stellar systems in the outer halo has further important implications for constraining the mass of the Milky Way (Watkins et al. 2018; Gaia Collaboration et al. 2018b).

7. Discussion

The ratio of a system’s rotation amplitude and central velocity dispersion, A_{rot}/σ_0 , versus its ellipticity (Fig. 9) is a representative measure for the importance of its dynamic-morphological interaction (e.g., Davies et al. 1983). While we were able to compute a meaningful global velocity dispersion for our two target GCs, the overall small number of sample stars aggravated a precise derivation of a dispersion profile, and the measurement of the central velocity dispersion σ_0 in our probabilistic fitting should be taken with caution. However, a radial dispersion gradient as seen in most GCs, e.g., when following the common Plummer profile (Mackey et al. 2013; Cordero et al. 2017), can be assumed. Moreover, many GCs are well described by a truncated King (1966) profile, which is essentially flat within a few core radii. Thus we can state the measured, global velocity dispersion as a lower limit of σ_0 , as is indeed realized in our rotational analysis.

Despite the, overall, large error bars the outer halo GC M 75 can be firmly considered as a slow rotator. It is worth noting that M 75 is very similar to NGC 4372 in terms of its A_{rot}/σ_0 ratio

and its ellipticity, although the latter is less massive and more metal poor (Kacharov et al. 2014; San Roman et al. 2015). In the parameter space of rotation vs. metallicity, M 75 falls fully in line with the majority of other Milky Way GCs, which is also consistent with its peculiar HB morphology. In turn, the very metal-poor NGC 6426 has a nominal, very large A_{rot}/σ_0 ratio of 0.8 ± 0.4 , although its large uncertainty renders it equally compatible with other GCs with slower rotation properties at comparable ellipticity. This cluster appears as an outlier, showing a more ordered dynamics given its low metallicity, which is, however, also seen in other metal-poor GCs below -2 dex. Here it is interesting to note that the minor axis of its, relatively large, flattening is consistent with the rotation axis found in the present study to within the uncertainties.

At their large distances in the halo, external tides from the Galactic disks are unlikely to play a significant dynamic role in shaping the outer halo clusters, and the observed, slow rotation favours internal dynamic processes as a cause for the mild observed flattening over tidal effects. Here, N-body simulations (e.g., Tiongco et al. 2017) show that, as GCs dynamically evolve in a tidal field, they become progressively dominated by random motions while losing angular momentum. Nonetheless, even after many relaxation times and accounting for mass loss from the GCs, they can still be characterized by non-negligible A_{rot}/σ_0 ratios.

Moreover, Kacharov et al. (2014) conjecture that most of the slow rotators are located on the younger, presumably accreted branch in the age-metallicity space (Marín-Franch et al. 2009). Coupled with other evidence such as its very eccentric orbit, its younger age compared to other GCs at the same metallicity, a large enrichment in the r -process elements (Kacharov et al. 2013), and the slow rotation pattern, it is likely that the more metal-rich of our targets, M 75, is a prime example of an accreted outer halo object, although the host to its accretion has still to be determined.

Acknowledgements. The authors are grateful to Eline Tolstoy for helpful comments on the FORS2 data set. The anonymous referee is thanked for a constructive and helpful report. This work was supported by Sonderforschungsbereich SFB 881 “The Milky Way System” (subproject A08) of the German Research Foundation (DFG).

References

- Armandroff, T. E. & Zinn, R. 1988, *AJ*, 96, 92
- Bastian, N., Lamers, H. J. G. L. M., de Mink, S. E., et al. 2013, *MNRAS*, 436, 2398
- Bastian, N., Cabrera-Ziri, I., & Salaris, M. 2015, *MNRAS*, 449, 3333
- Bastian, N. & Lardo, C. 2017, *ARA&A*, in press (arXiv:1712.01286)
- Baumgardt, H. 2017, *MNRAS*, 464, 2174
- Bellazzini, M., Bragaglia, A., Carretta, E., et al. 2012, *A&A*, 538, A18
- Bianchini, P., Varri, A. L., Bertin, G., & Zocchi, A. 2013, *ApJ*, 772, 67
- Binney, J. 2005, *MNRAS*, 363, 937
- Çalışkan, Ş., Christlieb, N., & Grebel, E. K. 2012, *A&A*, 537, A83
- Carballo-Bello, J. A., Sollima, A., Martínez-Delgado, D., et al. 2014, *MNRAS*, 445, 2971
- Carollo, D., Beers, T. C., Lee, Y. S., et al. 2007, *Nature*, 450, 1020
- Carretta, E., Bragaglia, A., Gratton, R., D’Orazi, V., & Lucatello, S. 2009a, *A&A*, 508, 695
- Carretta, E., Bragaglia, A., Gratton, R., & Lucatello, S. 2009b, *A&A*, 505, 139
- Carretta, E., Bragaglia, A., D’Orazi, V., Lucatello, S., & Gratton, R. G. 2010a, *A&A*, 519, A71
- Carretta, E., Bragaglia, A., Gratton, R. G., et al. 2010b, *A&A*, 516, A55
- Catelan, M., Borissova, J., Ferraro, F. R., et al. 2002, *AJ*, 124, 364
- Chemel, A. A., Glushkova, E. V., Dambis, A. K., Rastorguev, A. S., & Yalyalieva, L. N. 2018, *Astrophys. Bulletin*, in press (arXiv:1804.07086)
- Chen, C. W. & Chen, W. P. 2010, *ApJ*, 721, 1790
- Cole, A. A., Smecker-Hane, T. A., Tolstoy, E., Bosler, T. L., & Gallagher, J. S. 2004, *MNRAS*, 347, 367

- Cordero, M. J., Hénault-Brunet, V., Pilachowski, C. A., et al. 2017, *MNRAS*, 465, 3515 e-prints
- Corwin, T. M., Catelan, M., Smith, H. A., et al. 2003, *AJ*, 125, 2543
- Cutri, R. M., Skrutskie, M. F., van Dyk, S., et al. 2003, 2MASS All Sky Catalog of point sources.
- Davies, R. L., Efstathiou, G., Fall, S. M., Illingworth, G., & Schechter, P. L. 1983, *ApJ*, 266, 41
- Decressin, T., Meynet, G., Charbonnel, C., Prantzos, N., & Ekström, S. 2007, *A&A*, 464, 1029
- Dehnen, W. & Binney, J. 1998, *MNRAS*, 294, 429
- D’Ercole, A., Vesperini, E., D’Antona, F., McMillan, S. L. W., & Recchi, S. 2008, *MNRAS*, 391, 825
- Dias, B., Barbuy, B., Saviane, I., et al. 2015, *A&A*, 573, A13
- Dotter, A., Sarajedini, A., & Anderson, J. 2011, *ApJ*, 738, 74
- Ferraro, F. R., Mucciarelli, A., Lanzoni, B., et al. 2018, *ApJ*, in press (arXiv:2018.08618)
- Forbes, D. A. & Bridges, T. 2010, *MNRAS*, 404, 1203
- Foreman-Mackey, D., Hogg, D. W., Lang, D., & Goodman, J. 2013, *PASP*, 125, 306
- Fraternali, F., Tolstoy, E., Irwin, M. J., & Cole, A. A. 2009, *A&A*, 499, 121
- Gaia Collaboration, Brown, A. G. A., Vallenari, A., et al. 2018a, *ArXiv e-prints*
- Gaia Collaboration, Helmi, A., van Leeuwen, F., et al. 2018b, *ArXiv e-prints*
- Garnavich, P. M., Vandenberg, D. A., Zurek, D. R., & Hesser, J. E. 1994, *AJ*, 107, 1097
- Goodman, J. & Weare, J. 2010, *Communications in Applied Mathematics and Computational Science*, Vol. 5, No. 1, p. 65-80, 2010, 5, 65
- Gratton, R. G., Carretta, E., & Bragaglia, A. 2012, *A&A Rev.*, 20, 50
- Hanke, M., Koch, A., Hansen, C. J., & McWilliam, A. 2017, *A&A*, 599, A97
- Harris, W. E. 2010, *ArXiv e-prints*
- Hartwick, F. D. A. 1987, in *NATO Advanced Science Institutes (ASI) Series C*, Vol. 207, *NATO Advanced Science Institutes (ASI) Series C*, ed. G. Gilmore & B. Carswell, 281–290
- Kacharov, N., Koch, A., & McWilliam, A. 2013, *A&A*, 554, A81
- Kacharov, N., Bianchini, P., Koch, A., et al. 2014, *A&A*, 567, A69
- Kamann, S., Husser, T.-O., Dreizler, S., et al. 2018, *MNRAS*, 473, 5591
- Kayser, A., Hilker, M., Grebel, E. K., & Willemsen, P. G. 2008, *A&A*, 486, 437
- King, I. R. 1966, *AJ*, 71, 64
- Kleyna, J. T., Wilkinson, M. I., Evans, N. W., & Gilmore, G. 2004, *MNRAS*, 354, L66
- Koch, A., Wilkinson, M. I., Kleyna, J. T., et al. 2007, *ApJ*, 657, 241
- Koch, A., Côté, P., & McWilliam, A. 2009, *A&A*, 506, 729
- Koch, A. & Côté, P. 2010, *A&A*, 517, A59
- Koch, A., Hansen, C. J., & Kunder, A. 2017a, *A&A*, 604, A41
- Koch, A., Kunder, A., & Wojno, J. 2017b, *A&A*, 605, A128
- Koch, A., Hansen, T. T., & Kunder, A. 2018, *A&A*, 609, A13
- Kraft, R. P. & Ivans, I. I. 2003, *PASP*, 115, 143
- Kravtsov, V., Alcaíno, G., Marconi, G., & Alvarado, F. 2007, *A&A*, 469, 529
- Lardo, C., Pancino, E., Bellazzini, M., et al. 2015, *A&A*, 573, A115
- Mackey, A. D. & Gilmore, G. F. 2004, *MNRAS*, 355, 504
- Mackey, A. D., Da Costa, G. S., Ferguson, A. M. N., & Yong, D. 2013, *ApJ*, 762, 65
- Majewski, S. R., Kunkel, W. E., Law, D. R., et al. 2004, *AJ*, 128, 245
- Marín-Franch, A., Aparicio, A., Piotto, G., et al. 2009, *ApJ*, 694, 1498
- Martocchia, S., Cabrera-Ziri, I., Lardo, C., et al. 2018, *MNRAS*, 473, 2688
- Milone, A. P., Piotto, G., Renzini, A., et al. 2017, *MNRAS*, 464, 3636
- Osborn, W. 1971, *The Observatory*, 91, 223
- Pasquini, L., Avila, G., Blecha, A., et al. 2002, *The Messenger*, 110, 1
- Pillepich, A., Madau, P., & Mayer, L. 2015, *ApJ*, 799, 184
- Pryor, C. & Meylan, G. 1993, in *Astronomical Society of the Pacific Conference Series*, Vol. 50, *Structure and Dynamics of Globular Clusters*, ed. S. G. Djorgovski & G. Meylan, 357
- Robin, A. C., Reylé, C., Derrière, S., & Picaud, S. 2003, *A&A*, 409, 523
- Rutledge, G. A., Hesser, J. E., & Stetson, P. B. 1997a, *PASP*, 109, 907
- Rutledge, G. A., Hesser, J. E., Stetson, P. B., et al. 1997b, *PASP*, 109, 883
- Salaris, M. & Weiss, A. 2002, *A&A*, 388, 492
- San Roman, I., Muñoz, C., Geisler, D., et al. 2015, *A&A*, 579, A6
- Searle, L. & Zinn, R. 1978, *ApJ*, 225, 357
- Sohn, S. T., Watkins, L. L., Fardal, M. A., et al. 2018, *ApJ*, submitted (arXiv:1804.01994)
- Tiongco, M. A., Vesperini, E., & Varri, A. L. 2017, *MNRAS*, 469, 683
- Tiongco, M. A., Vesperini, E., & Varri, A. L. 2018, *MNRAS*, 475, L86
- Vesperini, E., McMillan, S. L. W., D’Antona, F., & D’Ercole, A. 2013, *MNRAS*, 429, 1913
- Vogt, S. S., Mateo, M., Olszewski, E. W., & Keane, M. J. 1995, *AJ*, 109, 151
- Walker, M. G., Mateo, M., Olszewski, E. W., et al. 2006, *AJ*, 131, 2114
- Walker, M. G., Mateo, M., Olszewski, E. W., Sen, B., & Woodroffe, M. 2009, *AJ*, 137, 3109
- Watkins, L. L., van der Marel, R. P., Sohn, S. T., & Evans, N. W. 2018, *ArXiv*